

Comparison of two basic types of interferometers in a Silicon On Insulator platform

VICTOR FARACI,¹

Submarine Line Terminal Equipment Department, Alcatel Submarine Networks, Les Ulis, France
victor.faraci@asn.com

Abstract: This report compares the transmission loss, the FSR and the extinction ratio of two different types of interferometers to be manufactured in a silicon-on-insulator (SOI) platform. Michelson interferometers (MI) will be made of Y-Branched. Mach-Zehnder Interferometers (MZI) will be composed of either Y-Branched or Broadband Directional Couplers (BDC). Only 500 nm width strip silicon waveguides are considered and mainly quasi-TE mode studied. Measurements will be compared to corner analysis and Monte-Carlo simulations.

1. Introduction

The main goal for following this course is to get a general overview of the full fabrication processes of a Photonic Integrated Circuit (PIC) chip. A focus on the design rules to minimise manufacturing variabilities, to facilitate measurements and analysis at wafer level and, to anticipate packaging constraints would be of interest. This course is also an opportunity to understand the capabilities of some simulation and design PIC tools. At first glance, first applications would be dedicated to Telecom ones as I work in this domain.

In this report, we will compare the performances of MZI composed with BDC or Y couplers. All of them have been designed for the same Free Spectral Range (FSR) of about 5 nm. Directional couplers are known to have a weak extinction ratio and to be wavelength selective. In contrary, Y branch couplers should exhibit a higher extinction ratio and less wavelength sensitivity. A focus on comparing the Extinction Ratios (ER) vs coupler types will be made if manufacturing variabilities will be neglectable enough. Two identical MIs equipped with Y branches and the same FSR as MZI ones are also submitted. Finally, two grating couplers back-to-back connected will allow to estimate their transmission spectrum. One pair is designed for Transverse Electric (TE) mode and the other for Transverse Magnetic (TM) one. Due to lack of space in this first design attempt, TM mode will be studied only for MZI structures with Y couplers. All the other circuits will be only TE designed.

2. Theory

2.1 Imbalanced Mach-Zehnder Interferometer

MZI consists of splitting the input light into two paths and then recombine them to interfere. Inside PICs, the split light will travel through two waveguides, generally with identical material properties and geometry. Their relative phase will determine the level of interference. In passive MZI without any electrode, it is fixed by the waveguide's length difference (namely imbalanced MZI) and temperature. Structures with electrodes along the waveguides will allow active control. In Telecom field, main applications are optical switches such as Thermo-optics [1, 2], PN Depletion modulators based on Plasma dispersion [3, 4] and optical filtering [5, 6]. MZI are also used in other application fields such as biosensors and spectroscopy.

Let us consider a simple model based on the plane-wave free-space beam-splitter as well described in chapter 4.3 of [7]. It can be applied in single-mode waveguides by only considering

the total field intensity within each waveguide but not the field distribution within them. In this model, splitting and combining functions are achieved with Y-Branched. A schematic of the structure is represented in Fig. 1.

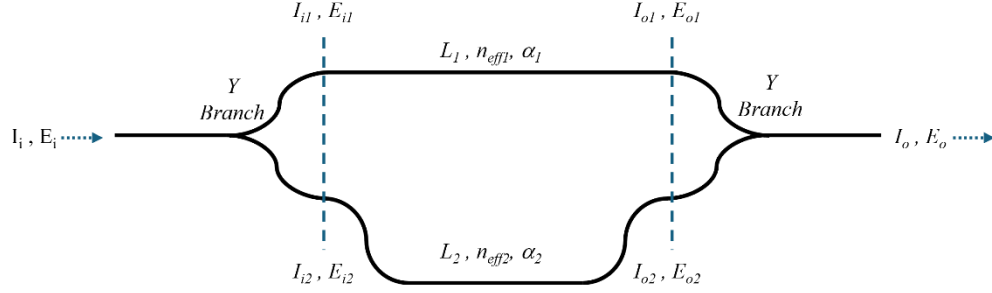


Fig. 1 Imbalanced MZI layout example composed of Y branch as splitter/combiner

At MZI input, the vectorial electrical field E_i is considered equally split into the two branches

$$E_{i1} = E_{i2} = \frac{E_i}{\sqrt{2}} \quad (1)$$

The intensity of the wave is equal to the square of the module of the electric field,

$$I_i = |E_i|^2 \quad (2)$$

leading to

$$I_{i1} = I_{i2} = \frac{I_i}{2} \quad (3)$$

The light propagation through respectively both top and bottom waveguides (according to Fig. 1) is governed by:

- their component of the wave vector along the propagation axis, namely propagation constant

$$\beta_1 = \frac{2\pi n_{eff1}}{\lambda} \quad (4)$$

$$\text{And } \beta_2 = \frac{2\pi n_{eff2}}{\lambda} \quad (5)$$

with n_{eff1} and n_{eff2} respectively the top and bottom waveguide effective indexes.

- their length L_1 and $L_2 = L_1 + \Delta L$
- their propagation loss α_1 and α_2 for intensity
- or for the electric field $\frac{\alpha_1}{2}$ and $\frac{\alpha_2}{2}$

When recombining into the output Y-Branch coupler the waves from the two waveguides E_{o1} & E_{o2} , the MZI output electrical field is expressed as follow:

$$E_o = \frac{1}{\sqrt{2}}(E_{o1} + E_{o2}) = \frac{E_i}{2}(e^{-i\beta_1 L_1 - \frac{\alpha_1}{2} L_1} + e^{-i\beta_2 L_2 - \frac{\alpha_2}{2} L_2}) \quad (6)$$

Therefore, the output intensity is:

$$I_o = \frac{I_i}{4} \left| e^{-i\beta_1 L_1 - \frac{\alpha_1}{2} L_1} + e^{-i\beta_2 L_2 - \frac{\alpha_2}{2} L_2} \right|^2 \quad (7)$$

If the attenuation of the waveguides is neglected i.e. $\alpha_1 = \alpha_2 = 0$, the expression of the intensity at the output of the MZI is simplified to:

$$I_o = \frac{I_i}{2} [1 + \cos(\beta_1 L_1 - \beta_2 L_2)] \quad (8)$$

When the two waveguides have the same material properties and geometry (except length) i.e. identical effective indexes $n_{eff1} = n_{eff2} = n_{eff}$, the intensity at the output of the imbalanced MZI varies sinusoidally with wavelength as depicted in Fig. 2 and follows the expression:

$$I_o(\lambda) = \frac{I_i}{2} \left[1 - \cos\left(\frac{2\pi n_{eff}}{\lambda} \Delta L\right) \right] \quad (9)$$

For balanced MZI ($\Delta L = 0$), one can note that $I_o = I_i$.

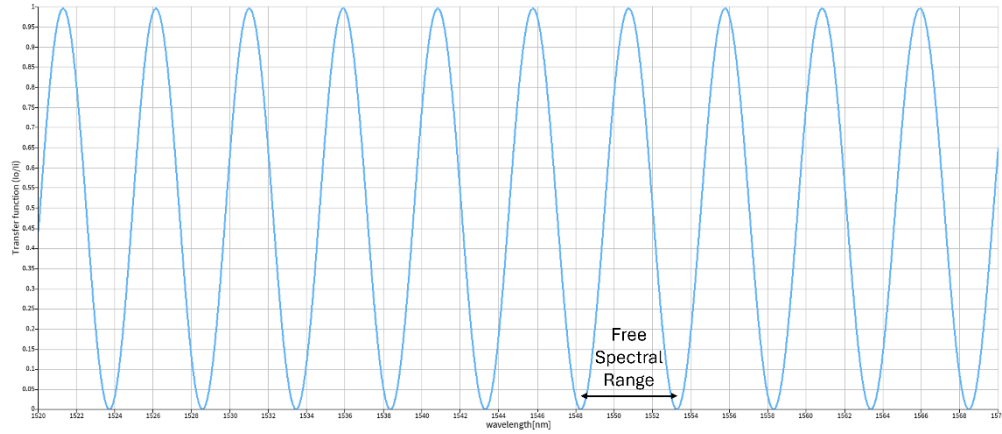


Fig. 2 Transfer function of an imbalanced MZI with about 5 nm FSR
 $n_{eff}(1550nm) = 2.441, n_g(1550nm) = 4.195, \Delta L = 114.2\mu m$

The period of this transfer function is named Free Spectral Range. In a dispersive medium, we must consider the group index for an interferometer. According to chapter 3.2.9 of [7], group index is related to effective index by:

$$n_g(\lambda) = n_{eff}(\lambda) - \lambda \frac{dn_{eff}}{d\lambda} \quad (10)$$

And FSR is expressed as follows:

$$FSR[Hz] = \frac{c}{n_g \Delta L} \quad (11)$$

or

$$FSR[m] = \frac{\lambda^2}{n_g \Delta L} \quad (12)$$

With c the speed of light in vacuum.

2.2 Imbalanced Michelson interferometer

MIs designed in PIC generally follows the architecture shown in Fig. 3 or in [11]. The light is split into two waveguides with a 2x2 directional coupler (DC). Principle and theory of DC can be found in chapter 4.1 of [7] or in [8]. This DC could also be adiabatic for larger optical bandwidth or a Multi-Mode Interferometer coupler (MMI) [9]. Both waveguides are terminated by a loop (typically a Y-branch looped back with the same waveguide as elsewhere in the PIC). The mirror light is then coupled back in the directional coupler. Therefore, the same interferometer behaviour as for MZM is obtained with a waveguide length difference twice smaller than in MZI i.e. $\Delta L/2$. MIs are then more compact than MZIs. The disadvantage is that they do not take advantage of travelling wave electrodes leading to a higher drive voltage than Mach-Zehnder Modulator (MZM). Nevertheless, a design based on folded MZI show much lower driving voltage [10].

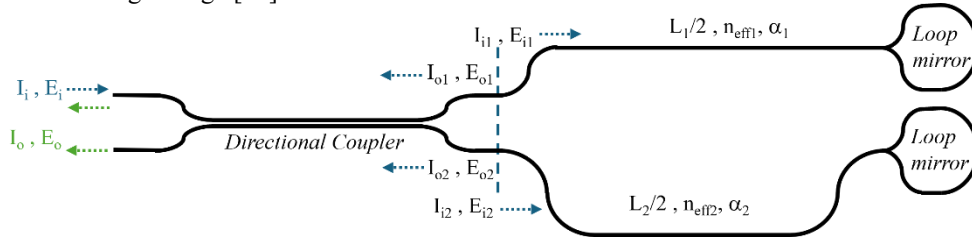


Fig. 3 Imbalanced Michelson Interferometer layout example

3.2 Couplers

In this work, BDC and Y-Branch couplers have been used.

Extinction Ratio (ER) of an interferometer is defined as the ratio of the maximum and minimum intensities of respectively the constructive and destructive interferences. It is known that BDC exhibit weaker ER than Y-Branch couplers, but theory has not been studied here. Nevertheless, from (7) we can see that the maximum constructive and destructive interferences cannot be achieved if the propagation losses of the two branches or if the coupling ratio are not equal.

3. Modelling and simulation

This study focussed only on a rectangular strip waveguide with 500 nm width and the typical 220 nm height used in the Silicon PIC industry. The differential length of all the MZIs has been set around $\Delta L = 114\mu\text{m}$ to get about 5 nm FSR at 1550 nm. For MIs, ΔL has been divided by two to remain with 5 nm FSR.

3.1 Mode Characteristics

Ansys Lumerical MODE software [12] has been used to simulate the mode profiles and characteristics of the desired waveguide. First mode is quasi-TE polarised and second one quasi-TM.

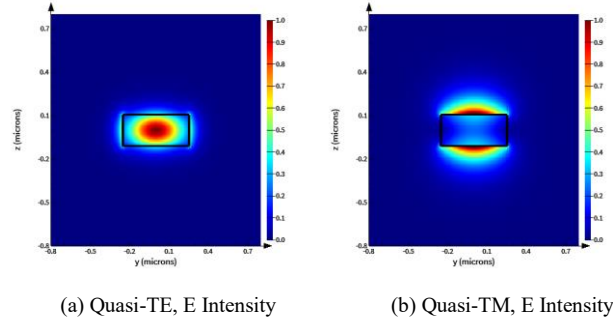


Fig. 4 shows the spatial electric field intensities of TE & TM polarisations, the two fundamental modes at 1550 nm. In Electric field intensity at 1550 nm for fundamental (a) TE mode and (b) TM mode Si/SiO₂ 500 x 220 nm strip waveguide

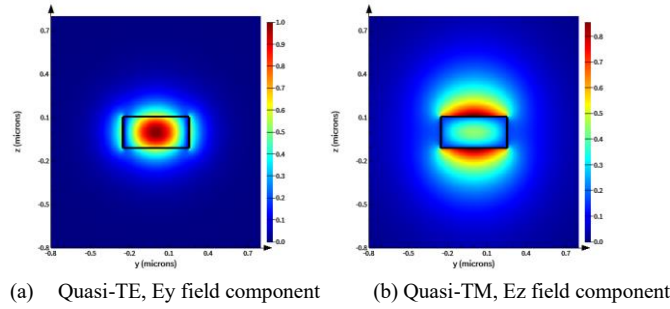


Fig. 5, we can see the discontinuities in the electric field at the Si/SiO₂ interface as expected from the boundary conditions in Maxwell's equations.

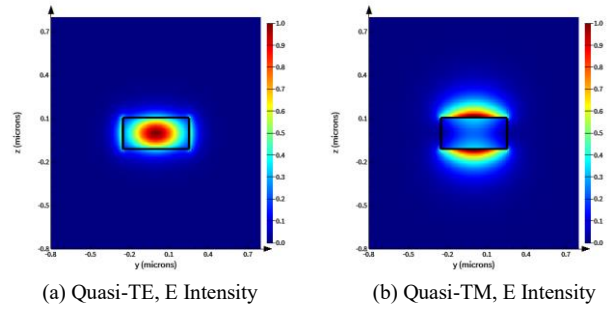


Fig. 4 Electric field intensity at 1550 nm for fundamental (a) TE mode and (b) TM mode Si/SiO₂ 500 x 220 nm strip waveguide

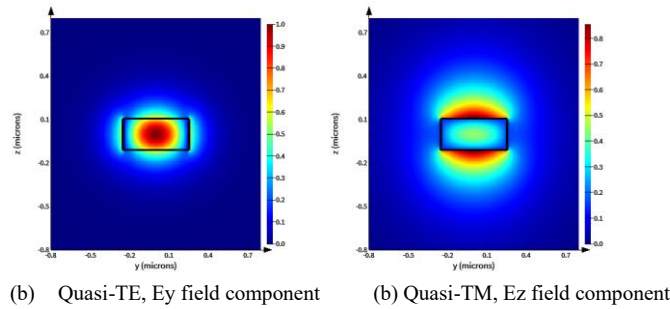


Fig. 5 Electric field component at 1550 nm for fundamental (a) TE mode along y axis and, (b) TM mode along z axis, Si/SiO₂ 500 x 220 nm strip waveguide

The effective and group indexes across wavelength range 1500-1600 nm are calculated for the two fundamental modes and plotted in Fig. 6 and Fig. 7.

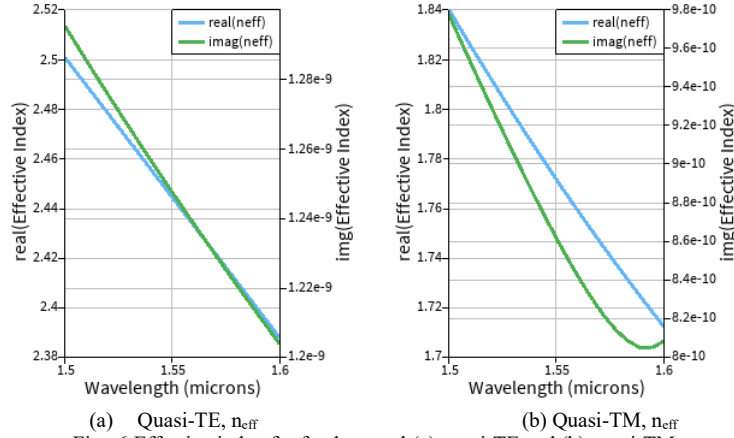


Fig. 6 Effective index for fundamental (a) quasi-TE and (b) quasi-TM Si/SiO₂ 500 x 220 nm strip waveguide

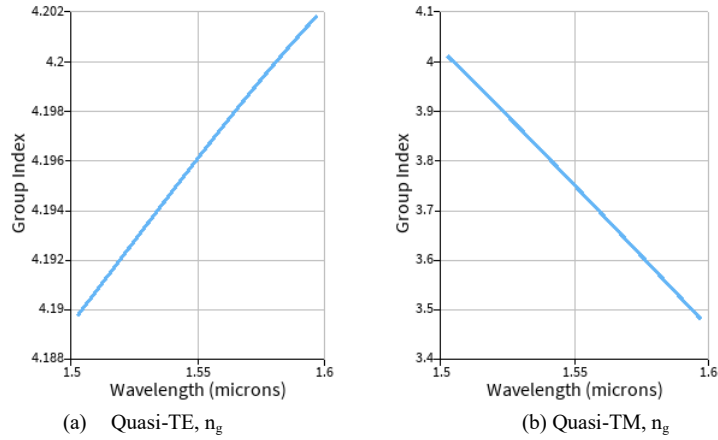


Fig. 7 Group index for fundamental (a) quasi-TE and (b) quasi-TM Si/SiO₂ 500 x 220 nm strip waveguide

The effective index n_{eff} can be expressed as a second order Taylor expansion centred around λ_0 :

$$n_{eff}(\lambda) = n'_{eff1} + n'_{eff2}(\lambda - \lambda_0) + n'_{eff3}(\lambda - \lambda_0)^2 \quad (13)$$

In our case, λ_0 is set to be in the middle of the simulation wavelength range i.e. 1550 nm. n_1 , n_2 and n_3 will allow to derive the effective index n_{eff} , the group index n_g , and the group velocity dispersion D as follows:

$$n_{eff} = n'_{eff1} \quad (14)$$

$$n_g = n'_{eff1} - n'_{eff2} \cdot \lambda_0 \quad (15)$$

$$D = -2 \cdot \lambda_0 \cdot \frac{n_{eff}^3}{c} \quad (16)$$

With c the speed of light in vacuum, D is typically quoted in units [ps/nm/km]

Using the data from the wavelength sweep simulations, we can derive the Taylor expansion for compact model of a 500 x 220 nm Si/SiO₂ strip waveguide.

With λ unit in μm , the fundamental quasi-TE mode can be modelled as:

$$n_{eff,TE}(\lambda[\mu\text{m}]) = 2.4444 - 1.13009(\lambda - 1.55) - 0.04175(\lambda - 1.55)^2 \quad (17)$$

And for the quasi-TM mode as

$$n_{eff,TM}(\lambda[\mu\text{m}]) = 1.7716 - 1.27649(\lambda - 1.55) + 1.81720(\lambda - 1.55)^2 \quad (18)$$

From (15), we can estimate that the group index 1550nm of a 500x220 nm Si/SiO₂ strip waveguide to be:

$$\begin{aligned} n_g(TE, 1550\text{nm}) &= 4.196 && \text{for fundamental Quasi TE mode} \\ n_g(TM, 1550\text{nm}) &= 3.750 && \text{for fundamental Quasi TM mode} \end{aligned}$$

3.2 Interferometers modelling and analysis

The mode parameters calculated previously with Ansys Lumerical MODE are then transferred to the Photonic Circuit Simulator Ansys Lumerical INTERCONNECT [13]. The different interferometers listed in Table 1 are modelled with the following elements available in EBeam library were used:

- Strip waveguide “ebeam_wg_strip_1550”
- Y branch “ebeam_Y_1550”
- Adiabatic 3dB coupler “ebeam_adiabatic_te1550”

Fibre to chip Grating Couplers (GC) have a strong wavelength dependency (see Fig. 24Fig. 31). Therefore, they have not been inserted in the simulation designs to do not perturb the transmission spectra of the different interferometers. During the analysis of the measurements performed on the design and manufactured chip, we will also remove in the spectra the envelop caused by the GCs.

Table 1 List of interferometers and elementary circuits simulated with interconnect and submitted for fabrication ($n_g=4.196$ for TE and $n_g=3.75$ for TM)

Circuit Type Label	Used coupler Type	Name in the Layout	Quantity in the cell	Mode	ΔL [μm]	FSR calculated at 1550nm [nm]
MZIY	Y branch	MZIYTE	2	TE	114.2	5.01
MZIY	Y branch	MZIYTM	2	TM	128.3	4.99
MZIBDC	BDC	MZIBDC	2	TE	114.2	5.01
MZIBDC-PSS	BDC Point Symmetric Splitter*	<i>Not implemented</i>	0	TE	114.2	5.01
MI	Y branch & BDC	Michelson	2	TE	57.1	5.01
Loopback	-	GCbtobTE	1	TE	-	-
Loopback	-	GCbtobTM	1	TM	-	-

* The two output ports of a BDC have 90° phase shift. Therefore, using a Point Symmetric Splitter at the MZI out (as shown in Fig. 8) will cancel it. To do so, it is flipped in both horizontal and vertical axes.

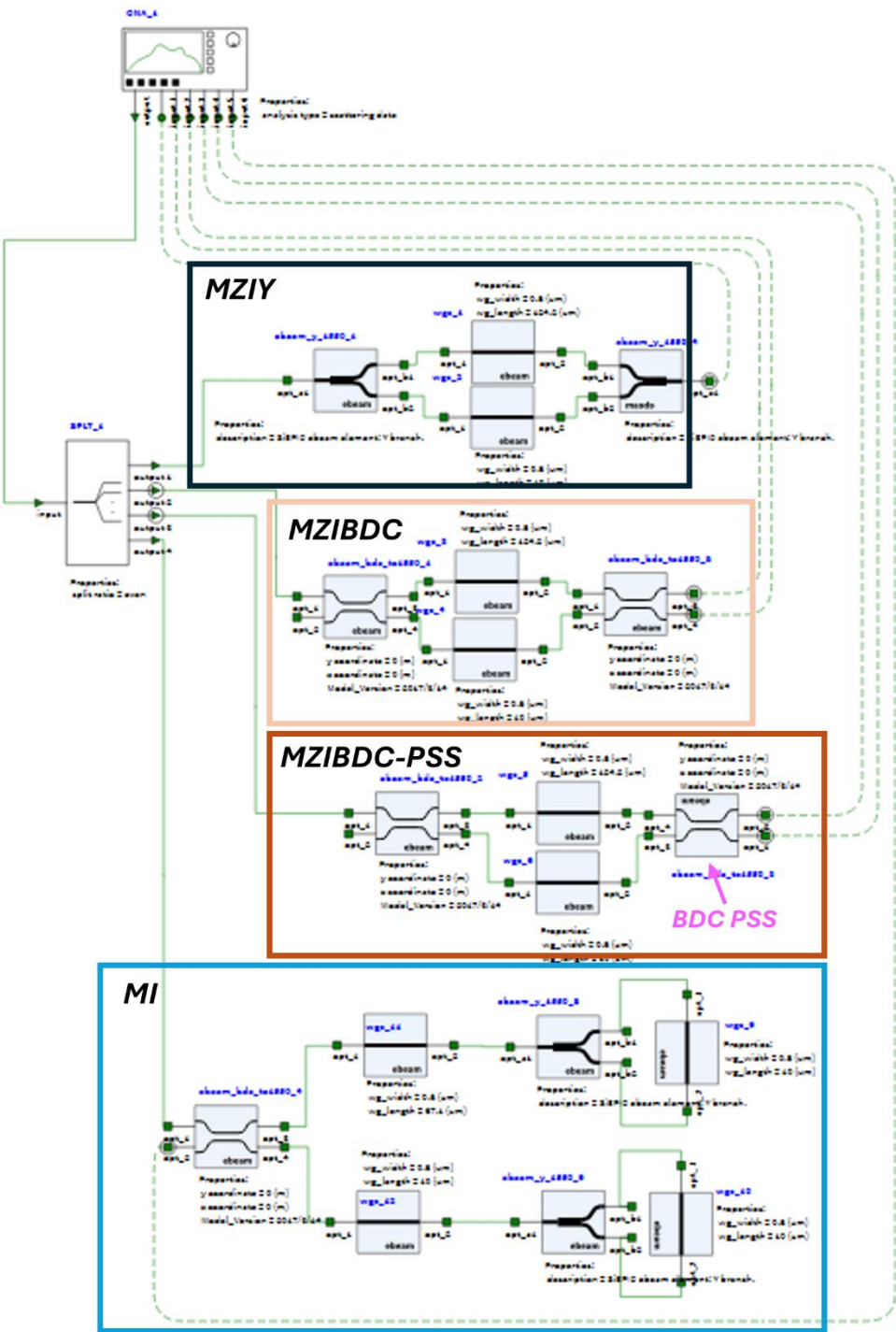


Fig. 8 Interferometer models simulated in Lumerical Interconnect

3.3 Simulation results

Transmission spectra of each circuit type listed in Table 1 are shown below. A wavelength step of 1 pm has been set (100,001 sampling points over 100nm). As shown in Fig. 8, a 1x4 ideal splitter has been introduced at the Optical Network Analyser in order to perform simultaneously the simulations of the four different circuits. Therefore, an offset of $6.02\text{dB} = 10\text{LOG}_{10}(4)$ must be removed from all following simulation spectra. You will then see that these four different interferometers exhibit extra Insertion Loss (IL) from 0.1 to 0.3dB.

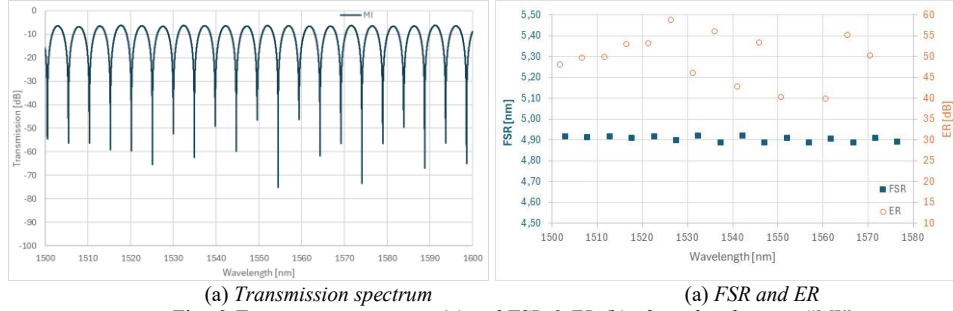


Fig. 9 Transmission spectrum (a) and FSR & ER (b) of simulated circuit "MI"

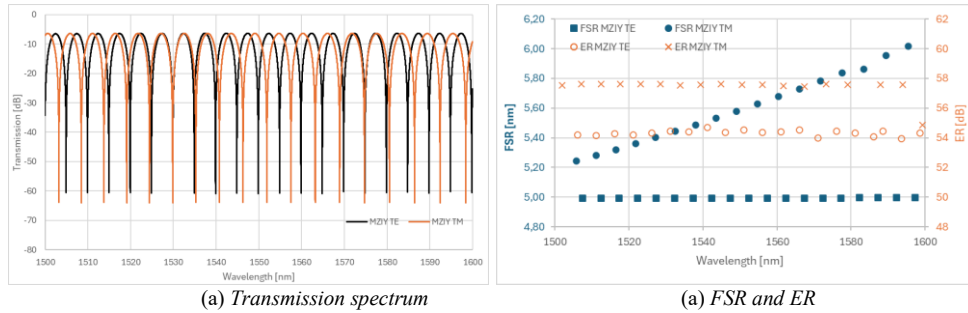


Fig. 10 Transmission spectrum (a) and FSR & ER (b) of simulated circuit "MZIY" for both polarisations TE & TM

TM mode a stronger dependency of FSR to wavelength than TE one, leading to a higher dispersive mode. One can see 3 dB higher ER for TM mode but I am unable to interpret it.

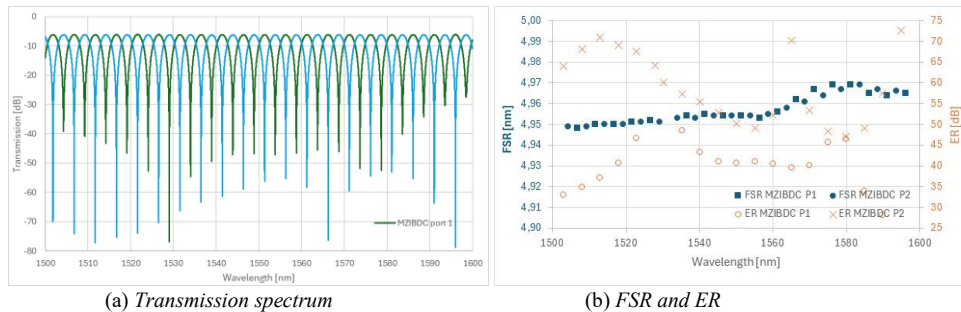


Fig. 11 Transmission spectrum (a) and FSR & ER (b) of simulated circuit "MZIBDC"

One can observe a difference on the average ER between the two ports close to 20dB and a strong wavelength dependency. It might be due to sampling and rounded artefact close to zero

(destructive interference) since the plot is in logarithmic scale. Nevertheless, it is not random over the spectrum of a same port. Fig. 12 compares spectra with 1 or 20 pm wavelength step. We will see if the manufactured circuits will exhibit the similar behaviour with probably less contrast due to measurement noise floor and manufacturing variabilities.

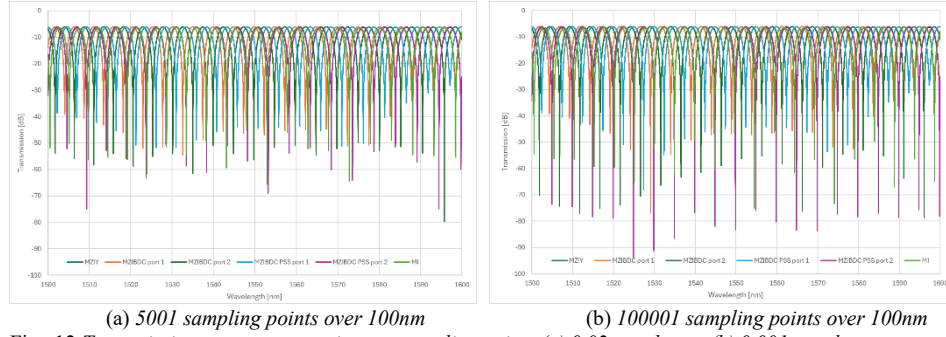


Fig. 12 Transmission spectra comparison vs sampling points (a) 0.02nm wl step, (b) 0.001nm wl step

MZDIBDC with PSS emphasise even more the ER difference between the two ports to about 36dB. Fig. 13 shows that FSR is also a bit more constant over the spectrum.

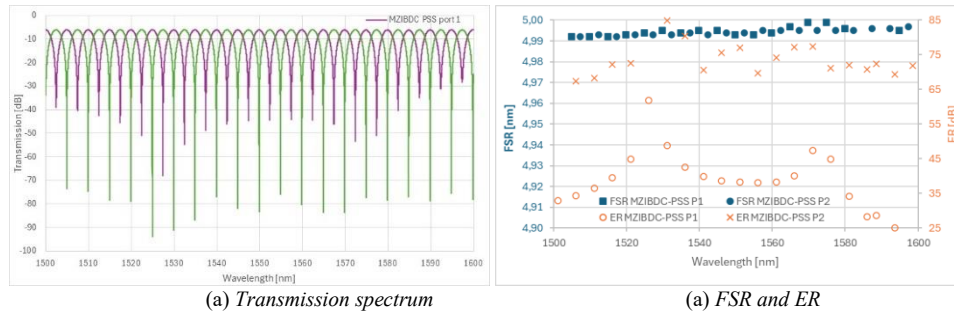


Fig. 13 Transmission spectrum (a) and FSR & ER (b) of simulated circuit “MZIBDC-PSS”

Transmission spectra in Fig. 14 (b) seems to show a higher ER of port 2 of the MZI structure with a PSS splitter compared to the one of “MZIBDC” structure. But ER of ports 1 of these two MZI are similar and show a pattern (

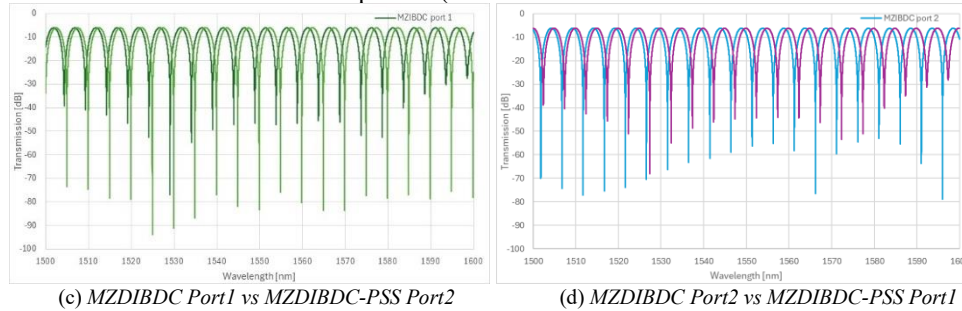
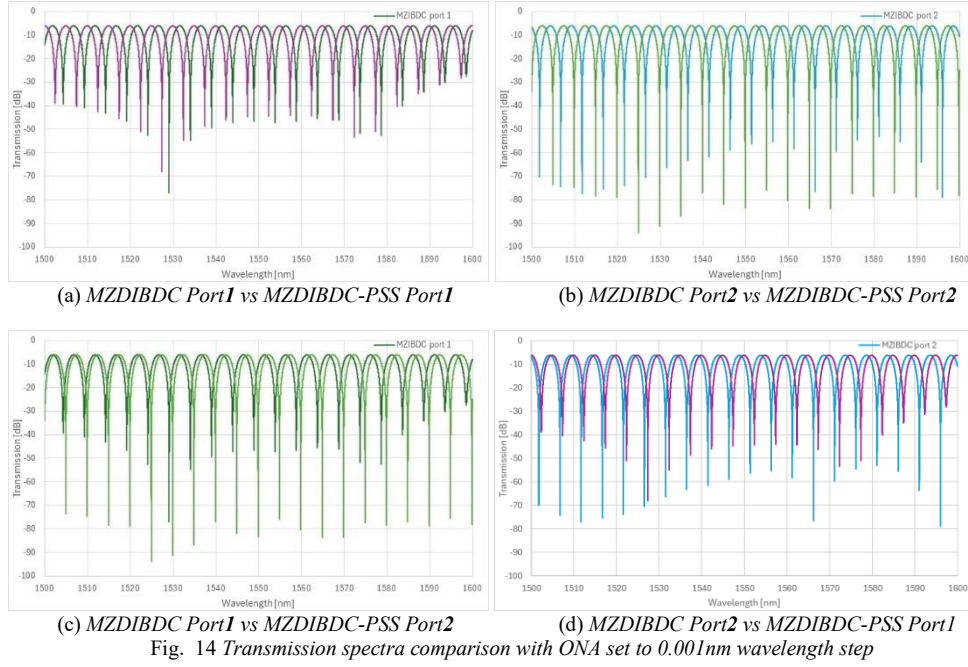
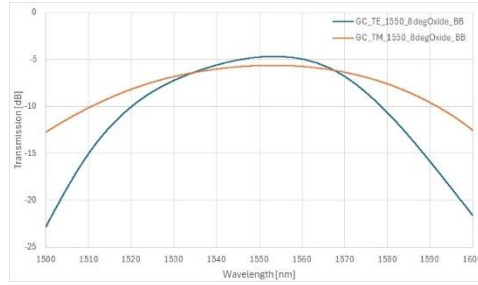


Fig. 14 (a)). One cannot exclude that this observation might be flawed by data sampling issue.



To allow easy and automatic transmission loss measurements at wafer level, we will connect our designed circuit to two Grating Couplers (for input and output light). Fig. 15 shows the transmission spectra of two TE polarised GC from EBeam library “GC_TE_1550_8degOxide_BB” in cascade and for TM “GC_TM_1550_8degOxide_BB”. One can see that TM GC has a much lower wavelength dependency at the expense of about 1dB higher minimum IL.



Equation (10) shows that FSR around a given wavelength is inversely proportional to the group index and ΔL . Therefore, with the calculated FSR from the transmission spectra measured on our fabricated chip, we will derive the group index at a given wavelength (assuming no error fabricated on ΔL). We will then compare it to Ansys Lumerical MODE simulation.

As example, we can calculate the FSR of the “MZIBDC” structure (with $114.2\mu\text{m}$ ΔL) to be 4.98nm FSR leading to a group index at 1550nm $n_g = \frac{\lambda^2}{\text{FSR} \cdot \Delta L} = 4.228$.

3.4 Layout

The layout of the chip has been designed with KLayout software tool [14]. A space of 605 x 410 μm was allocated to each student. We had to follow some design rules to automatise measurements at wafer level such as all GC must be oriented to the right and, aligned vertically with 127 μm pitch when measuring the same elementary circuit. Because effective index of TM mode is lower than for TE, light is less confined. Therefore, to mitigate bend losses, TM guides have been designed with 15 μm radii rather than 5 μm for TE ones. To lower manufacturing variabilities, similar circuits have been located as close as possible. The circuit layout depicted in Fig. 16 is delimited by dashed lines in five different zones (four for each interferometer structure and one for GC loopback). Except for GCs, each zone is composed of two identical designs aligned vertically when possible. One can wonder if a horizontal alignment would have not reduced manufacturing variabilities since circuits will be closer.

I chose a simple GC loopback design without balanced interferometer but equipped with two quarter turns and a straight waveguide. This is to avoid the risk to estimate a wrong extra insertion loss due to phase mismatch between the two arms because of manufacturing variabilities.

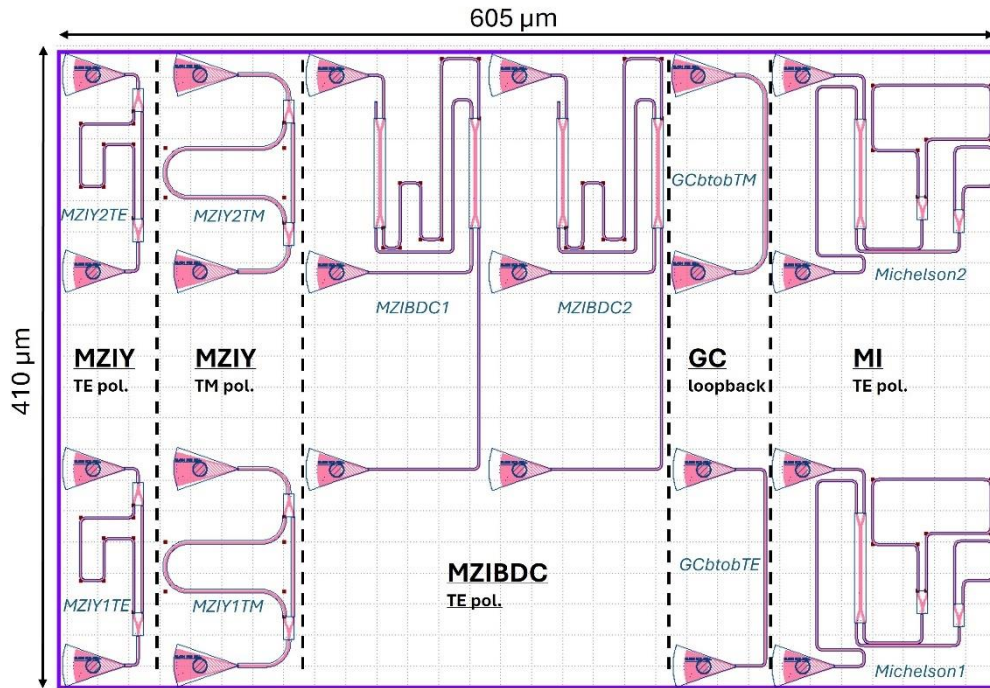


Fig. 16 Fabrication Design Layout

Table 2 List of fabricated devices

Chip cell zone	Label	ΔL [μm]
MZIY TE pol.	MZIY1TE	114.2
	MZIY2TE	114.2
MZIY TM pol.	MZIY1TM	128.3
	MZIY2TM	128.3
MZIBDC TE pol.	MZIBDC1	114.2
	MZIBDC2	114.2
GC Loopback	GCbtobTE	-
	GCbtobTM	-
MI TE pol.	Michelson1	57.1
	Michelson2	57.1

3.5 Manufacturing variabilities

Principle parameters that will affect the performances of our fabricated devices are the width and height of the waveguides. The height is mainly driven by the wafer quality. Whereas the width by the Electron Beam Lithography process (EBL).

Wafers are provided by SOITEC company located in Grenoble in France have the following main characteristics:

- 6" wafer diameter, prime grade
- Si thickness, mean = 219.2 nm
- Si thickness, 6 sigma = 23.4 nm (or +/- 3.9 nm, for one standard deviation)
- SiO₂ thickness, mean = 2994.5 nm
- SiO₂ thickness, 6 sigma = 6.3 nm

Concerning the waveguide width variations, main parameters are:

- Resist imperfections: age, sensitivity to exposure, viscosity as well as its spin coated process
- Exposure dose vs design
- Development process: removal of the resist, rinsing, drying and blowing. And quality of the chemicals.
- Silicon Etching: In our case, Si is removed with Inductive Coupled Plasma (ICP). It is also dependent on the process and quality of the chemicals.

The devices will be manufactured by the integrated photonics foundry Applied Nanotools [15]. One can consider a nominal waveguide width of 500nm with -30/+10nm variation.

3.5.1 Corner analysis

A rapid analysis to estimate the interferometer performance variation is to perform a corner analysis based on the waveguide geometry. This will affect the effective and group indexes leading respectively to peak wavelength shift and FSR variations.

In our case, we consider a nominal dimension of 219.2 x 500 nm. Using Ansys Lumerical MODE, we can derive the effective and group indexes for the nine "extreme" dimension variations that might happen during our fabrication. Results are given at 1550nm in Table 3. FSR and Peak central wavelength calculated at 1500 nm are highlighted in bold characters.

Table 3 Corner analysis, Si/SiO₂ strip waveguide, (a) TE & (b) TM polarised around 1550nm

	n1	n2	n3	n _{eff}	n _g	FSR [nm]	Peak wt [nm]
500nm x 219,2nm nominal	2,44132	-1,13167	-0,04041	2,44132	4,19541	5,01	1548,88
470nm x 215,3nm	2,35949	-1,20750	-0,03193	2,35949	4,23111	4,97	1548,58
470nm x 219,2nm	2,38924	-1,20071	-0,04134	2,38924	4,25034	4,95	1550,29
470nm x 223,1nm	2,40380	-1,19420	-0,05031	2,40380	4,25481	4,94	1550,93
500nm x 223,1nm	2,45574	-1,12486	-0,04735	2,45574	4,19927	5,01	1549,42
510nm x 223,1nm	2,47100	-1,10416	-0,04514	2,47100	4,18245	5,03	1550,48
510nm x 219,2nm	2,45661	-1,11101	-0,03860	2,45661	4,17868	5,03	1549,97
510nm x 215,3nm	2,44229	-1,11816	-0,03175	2,44229	4,17544	5,04	1549,50
500nm x 215,3nm	2,42698	-1,13875	-0,03312	2,42698	4,19204	5,02	1548,39
500nm x 220nm	2,44435	-1,13009	-0,04175	2,44435	4,19599	5,01	1550,80

Min n _g @ 1550nm	4,17544
Max n _g @ 1550nm	4,25481

	n1	n2	n3	n _{eff}	n _g	FSR [nm]	Peak wt [nm]
500nm x 219,2nm nominal	1,76532	-1,26202	1,83000	1,76532	3,72145	5,03	1551,31
470nm x 215,3nm	1,71732	-1,15741	1,93364	1,71732	3,51131	5,33	1551,63
470nm x 219,2nm	1,74411	-1,23056	1,90617	1,74411	3,65148	5,13	1553,95
470nm x 223,1nm	1,77055	-1,29585	1,85248	1,77055	3,77912	4,96	1545,32
500nm x 223,1nm	1,79280	-1,32398	1,76289	1,79280	3,84497	4,87	1554,16
510nm x 223,1nm	1,79994	-1,33328	1,73495	1,79994	3,86652	4,84	1549,88
510nm x 219,2nm	1,77224	-1,27211	1,80554	1,77224	3,74401	5,00	1546,79
510nm x 215,3nm	1,74405	-1,20252	1,85248	1,74405	3,60796	5,19	1553,90
500nm x 215,3nm	1,73749	-1,19169	1,87242	1,73749	3,58461	5,22	1548,06
500nm x 220nm	1,77160	-1,27649	1,81720	1,77160	3,75016	4,99	1546,23

Min n _g @ 1550nm	3,51131
Max n _g @ 1550nm	3,86652

We can also see n_{eff} and n_g plots over wavelength in Fig. 17 for TE mode and in Fig. 18 for TM one.

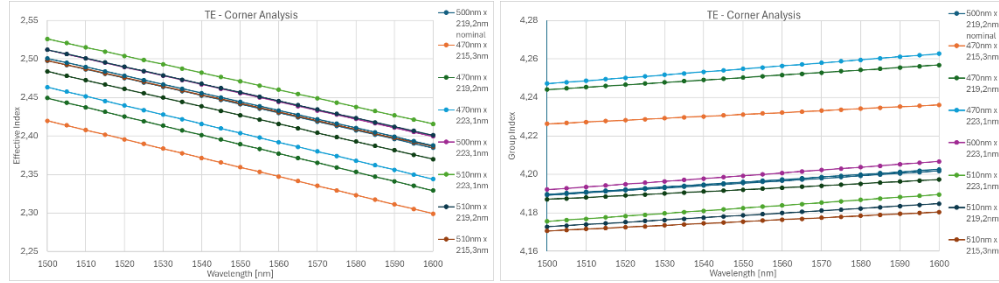


Fig. 17 Corner Analysis, TE mode, (a) effective index and (b) group index

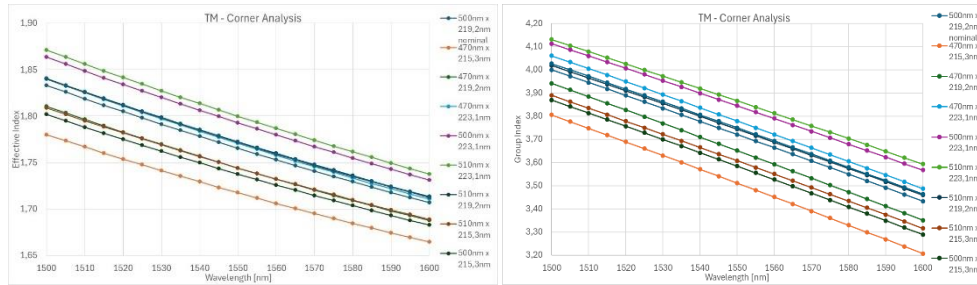


Fig. 18 Corner Analysis, TM mode, (a) effective index and (b) group index

Peak central wavelength estimated in the corner analysis has been derived from the effective index calculation. When the two arms of a MZI have the same effective index, their phase difference is expressed as:

$$\Delta\phi = \frac{2\pi}{\lambda} \Delta L \cdot n_{eff} \quad (19)$$

The interferometer is resonant (constructive interference) when the phase difference is a multiple of 2π :

$$\Delta\phi = m \cdot 2\pi \quad (20)$$

with $m \in \mathbb{Z}$

This conduct to a condition of resonance for the wavelength λ_m :

$$\lambda_m = \frac{\Delta L \cdot n_{eff}}{m} \quad (21)$$

3.5.2 Monte-Carlo simulation

A more accurate method to compare simulations to measured devices will be to run Monte-Carlo simulation. We used the settings proposed in KLayout for Applied Nanotools EBL process (see Table 4).

Table 4 Parameters for Monte-Carlo simulation

	Inside wafer variation			Wafer to wafer variation	
	Std. Dev [nm]	Correlation Length [m]		Std. Dev [nm]	
Width variation	1.132	12.23e-3	Width variation	5.0	
Height variation	0.585	8.72e-3	Thickness variation	3.0	

Simulations have been run assuming for 4 different wafers and 15 locations per wafer. One could wonder to rather increase the quantity of wafers since it has higher standard deviations. Monte-Carlo simulation is launched from KLayout but it is performed by Ansys Lumerical INTERCONNECT. Since the FSR of all devices is around 5nm at 1550nm, the wavelength range has been zoomed to 1540 – 1560 nm.

Table 5 shows FSR and Peak wavelength around 1550nm simulated with the Monte-Carlo statistics.

Table 5 Monte-Carlo simulation for the manufactured devices, 4 wafers, 15 locations/wafer, results around 1550nm

	Monte-carlo simulation					
	FSR [nm]			Peak wl [nm]		
	Min	Max	Av.	Min	Max	Av.
MZIYTE	4,72	5,33	5,01	1547,55	1542,44	1550,05
MZIYTM	4,68	5,06	4,79	1535,42	1539,85	1537,78
MZIBDCIN	4,93	5,27	4,78	1545,7	1559,92	1549,79
Michelson	3,91	5,75	4,95	1545,91	1550,83	1547,54

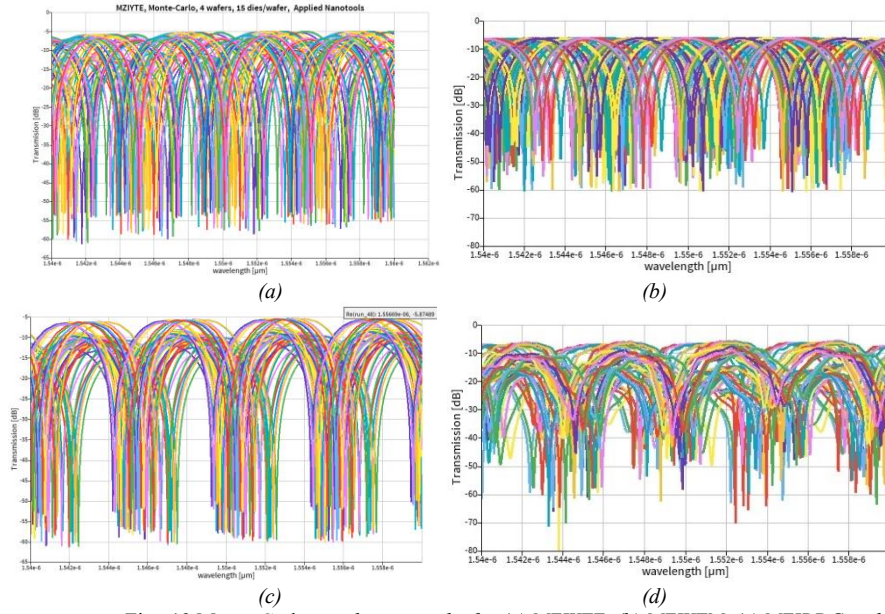


Fig. 19 Monte-Carlo simulation results for (a) MZIYTE, (b) MZIYTM, (c) MZIBDC and (d) Michelson

We cannot observe a strong difference between TE & TM MZIY structures.

The quality of the graph for the Michelson is poor nevertheless we can observe a much larger dispersion on FSR than for the other structures as confirmed in Table 5. The spectra exhibit also a fast ripple deforming the interferometric sinusoid. I was not enabled to locate the source of this noise using INTERCONNECT.

GCs transmission functions will also impair strongly response of the manufactured interferometers. Table 6 shows strong variation in minimum IL and peak wavelength for both TE & TM modes. Transmission spectra are also strongly wavelength dependent as seen in Fig. 20 & Fig. 21. One can note also about 1.7 nm periodic ripple for TE and 2.3 nm for TM. This IL dispersion will affect the interferometer responses.

Table 6 Monte-Carlo simulation for the loop-back GC, IL & Peak wl.

	Min. IL [dB]		Min. IL wl [nm]	
	Min	Max	Min	Max
GCbtobTE	4.99	7.67	1546.61	1562.74
GCbtobTM	5.68	6.19	1540.08	1561.90

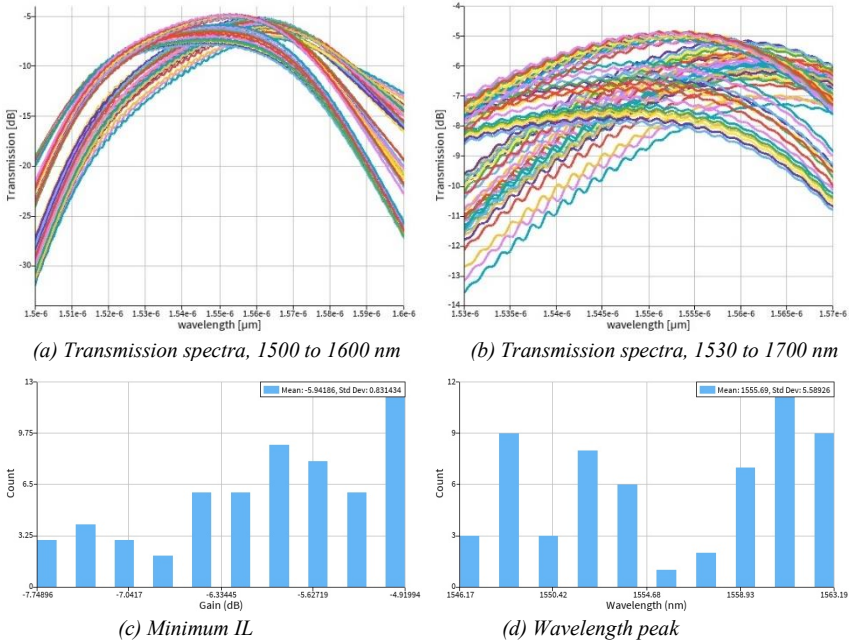


Fig. 20 Monte-Carlo simulation for the loop-back GC, TE mode, "GCbtoBTE"

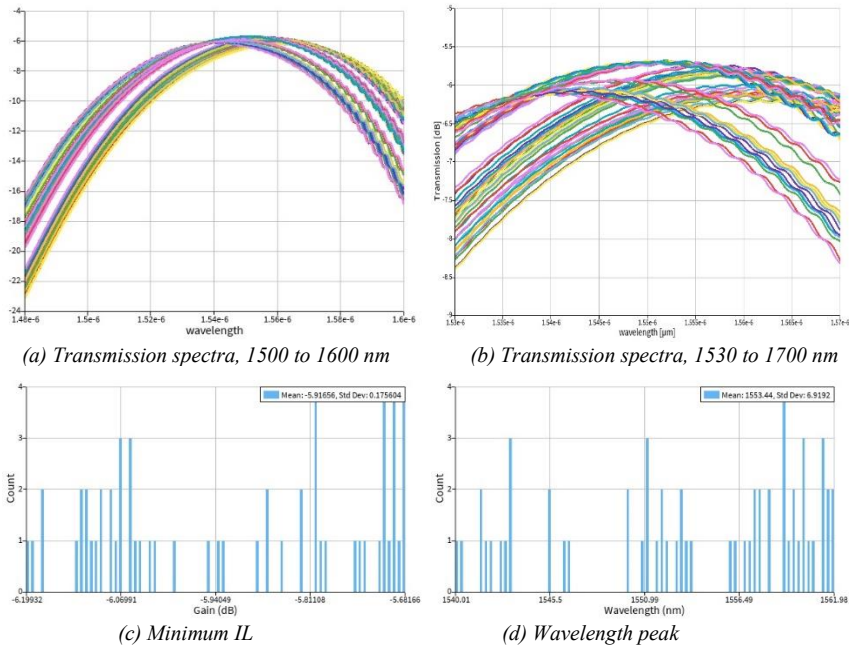


Fig. 21 Monte-Carlo simulation for the loop-back GC, TM mode, "GCbtoBTM"

Remark: the y scale in transmission spectra is different between TE & TM GCs

4. Fabrication (Applied Nanotools)

The photonic devices were fabricated using the NanoSOI MPW fabrication process by Applied Nanotools Inc. (<http://www.appliednt.com/nanosoi>; Edmonton, Canada) which is based on direct-write 100 keV electron beam lithography technology. Silicon-on-insulator wafers of 200 mm diameter, 220 nm device thickness and 2 μm buffer oxide thickness are used as the base material for the fabrication. The wafer was pre-diced into square substrates with dimensions of 25x25 mm, and lines were scribed into the substrate backsides to facilitate easy separation into smaller chips once fabrication was complete. After an initial wafer clean using piranha solution (3:1 $\text{H}_2\text{SO}_4:\text{H}_2\text{O}_2$) for 15 minutes and water/IPA rinse, hydrogen silsesquioxane (HSQ) resist was spin-coated onto the substrate and heated to evaporate the solvent. The photonic devices were patterned using a Raith EBP 5000+ electron beam instrument using a raster step size of 5 nm. The exposure dosage of the design was corrected for proximity effects that result from the backscatter of electrons from exposure of nearby features. Shape writing order was optimized for efficient patterning and minimal beam drift. After the e-beam exposure and subsequent development with a tetramethylammonium sulfate (TMAH) solution, the devices were inspected optically for residues and/or defects. The chips were then mounted on a 4" handle wafer and underwent an anisotropic ICP-RIE etch process using chlorine after qualification of the etch rate. The resist was removed from the surface of the devices using a 10:1 buffer oxide wet etch, and the devices were inspected using a scanning electron microscope (SEM) to verify patterning and etch quality. A 2.2 μm oxide cladding was deposited using a plasma-enhanced chemical vapour deposition (PECVD) process based on tetraethyl orthosilicate (TEOS) at 300°C. Reflectometry measurements were performed throughout the process to verify the device layer, buffer oxide and cladding thicknesses before delivery.

NB: Above text describing Applied Nanotools fabrication, chap4., has been copied from https://www.authorea.com/users/15604/articles/140161/_show_article

5. Experimental Data

Devices have been characterised with a custom-built automated test bench. It allows measurements at wafer level thanks to a fibre array aligned to the GCs of the devices. It is composed of one tuneable Laser source (equipped with Polarisation Maintaining Fibre, PMF) and three detectors (*Fig. 22, copied from EdX course*). Measurements have been performed from 1500 to 1580nm. TE ones with a wavelength step of 5 nm. For TM, a 90° rotation is used to inject the light into the TM GCs. The wavelength step was increased to 8 nm. All provided measurements are listed in Table 7. Please refer to Fig. 16 to find their location in the allocated chip cell. To get the maximum data count, when possible, the devices have been measured in both directions i.e. from Port x to Port x \pm 1 or -2/+1 and also from Port x \pm 1 or -2/+1 to Port x.

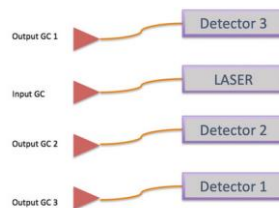


Fig. 22 Test-bench Fibre Array topology (copied from EdX course)

Table 7 Provided Data look-up table

Structure	Label	Detector #
MZIY TE mode	MZIY1TE1	3
	MZIY1TE2	2
	MZIY2TE1	3
	MZIY2TE2	2
MZIY TM mode	MZIY1TM1	3
	MZIY1TM2	2
	MZIY2TM1	3
	MZIY2TM2	No Data
MZIBDC TE mode	MZIBDC1IN2	3
	MZIBDC1IN3	1
	MZIBDC1IN3	2
	MZIBDC2IN2	3
	MZIBDC2IN3	1
	MZIBDC2IN3	2
Michelson TE mode	Michelson1In1	3
	Michelson1In2	2
	Michelson2In1	3
	Michelson2In2	2
GC Loopback TE mode	GCbtobTE1	3
	GCbtobTE2	2
GC Loopback TM mode	GCbtobTM1	3
	GCbtobTM2	2

5.1 TE Measurements

At first glance, Fig. 23 shows that almost all the devices follow the spectral envelop of the GCs.

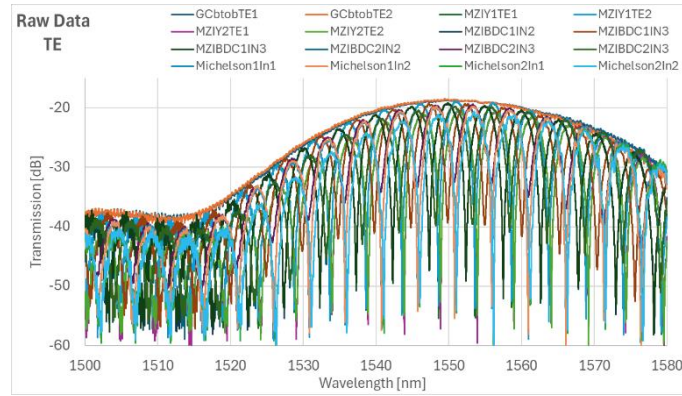


Fig. 23 Raw measurements, TE mode, all devices

5.1.1 GCbtobTE

Both measurements of Fibre GC are close enough to extract a fit based on the average of the two spectra smoothed with $\pm 1\text{nm}$ sliding average (Fig. 24). One should note that this GC loopback exhibits more than 11dB extra IL compared to Monte-Carlo simulations (Table 6). The centre wavelength 1549.9 nm is within simulation dispersion range. This GC smoothing will be subtracted to all our device measurements. This will not affect our FSR and ER analysis. We will call them “Baseline corrected”.

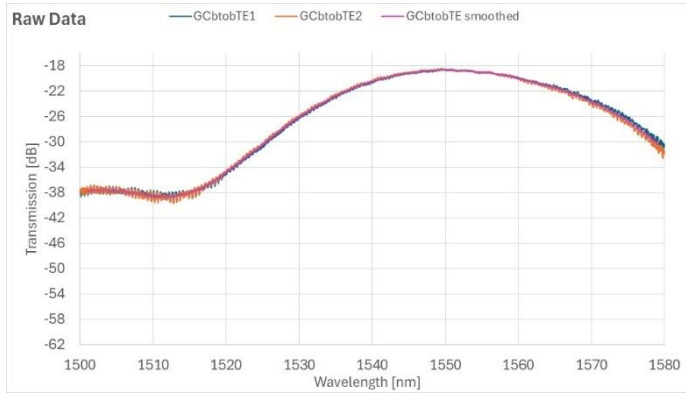
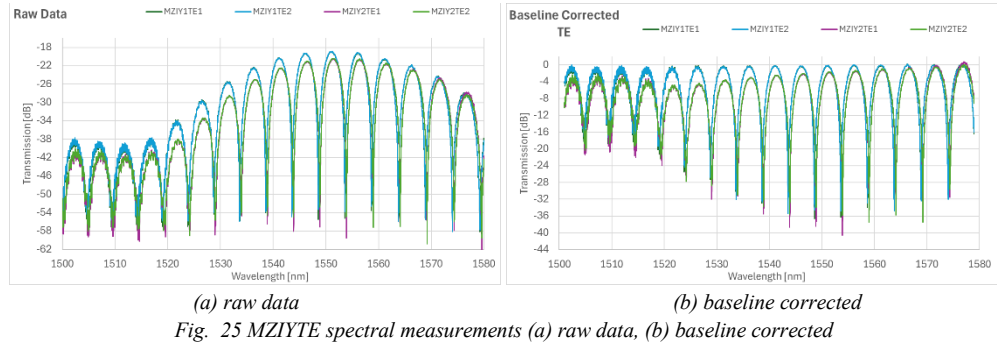


Fig. 24 GCbtoBTE loopback spectral measurements

5.1.2 MZIYTE

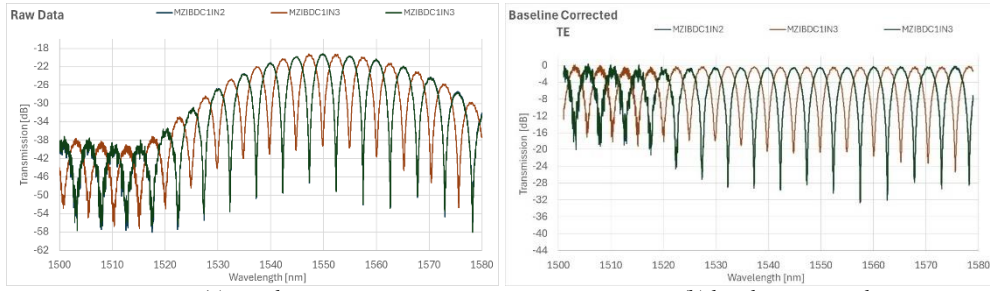
One can see that min ILs are slightly positive (lower than 0.8dB) meaning that the grating for these devices should have few more attenuation than removed.



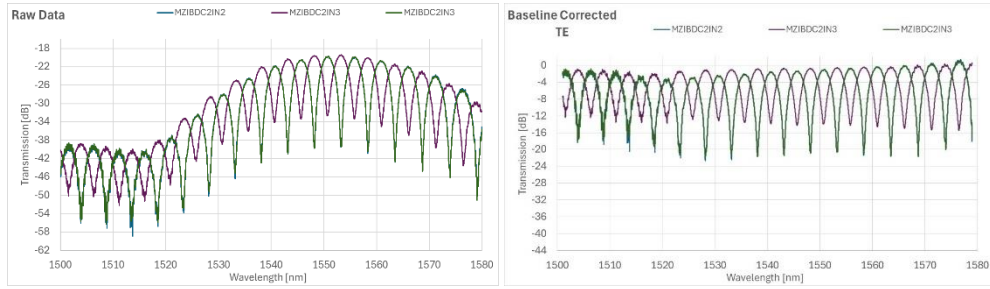
(a) raw data (b) baseline corrected
Fig. 25 MZIYTE spectral measurements (a) raw data, (b) baseline corrected

5.1.3 MZIBDC

As expected, MZIBDCIN2 detector3 and MZIBDCIN3 detector2 superimpose. The minimum IL for baseline corrected is still slightly positive, +0.3dB for MZIBDC1 and +1.3dB for MZIBDC2. One can note observe tha ERs are much lower for MZIBDC2.



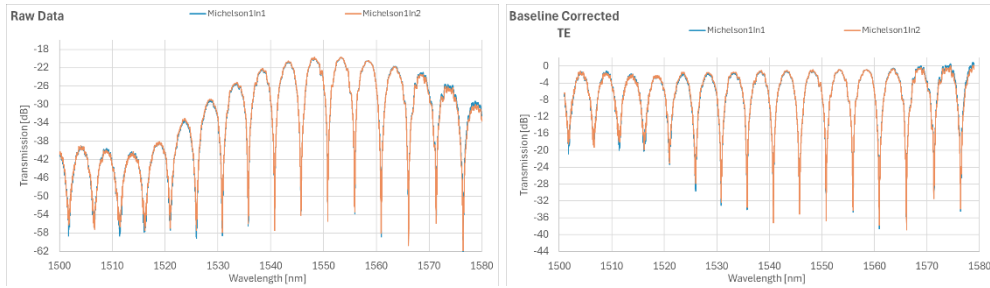
(a) raw data (b) baseline corrected
Fig. 26 MZIDBC1 spectral measurements (a) raw data, (b) baseline corrected



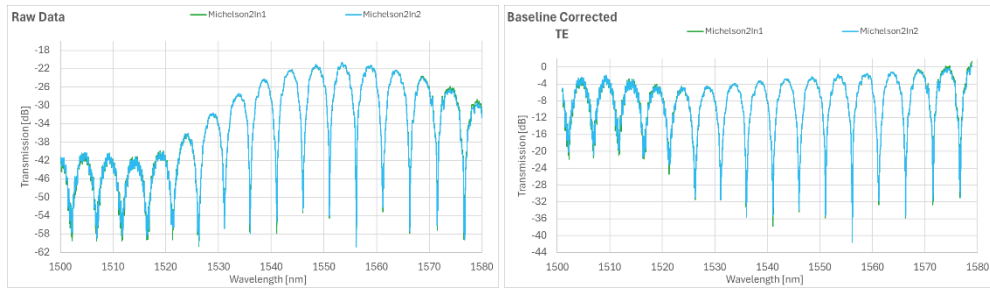
(a) raw data (b) baseline corrected
Fig. 27 MZIDBC2 spectral measurements (a) raw data, (b) baseline corrected

5.1.4 Michelson

Baseline corrected spectra (Fig. 28 Fig. 29) is not flat. It seems the GC are shifted to higher wavelengths compared to our reference loopback baseline.



(a) raw data (b) baseline corrected
Fig. 28 Michelson1 spectral measurements (a) raw data, (b) baseline corrected



(a) raw data (b) baseline corrected
Fig. 29 Michelson2 spectral measurements (a) raw data, (b) baseline corrected

5.2 TM Measurements

Fig. 30 shows that MZIY1 device fits well envelop of the TM Loopback GCs. For MZIY2, we can suppose that the GCs are shifted towards lower wavelenthns.

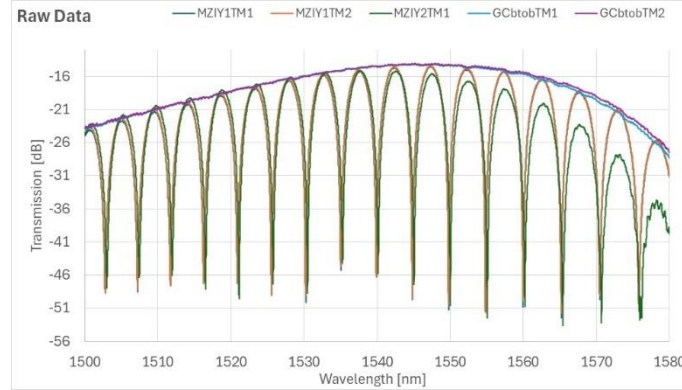


Fig. 30 Raw measurements, TM mode, all devices

5.2.1 GCbtoBTM

As for TE, measurements of Fibre GC are close enough to extract a fit based on the average of the two spectra smoothed with $\pm 1\text{nm}$ sliding average (*Fig. 31* *Fig. 24*). Also, GC loopback exhibits 8 to 9 dB higher IL compared to Monte-Carlo simulations (Table 6). The centre wavelength 1548.1 nm matches with the simulation deviation range. This GC smoothing will be subtracted to both MZIY devices measurements.

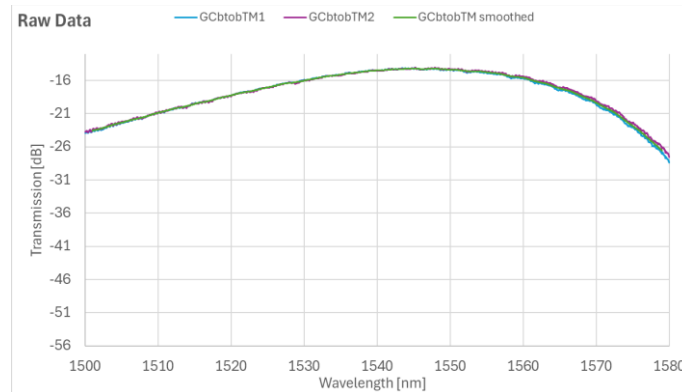
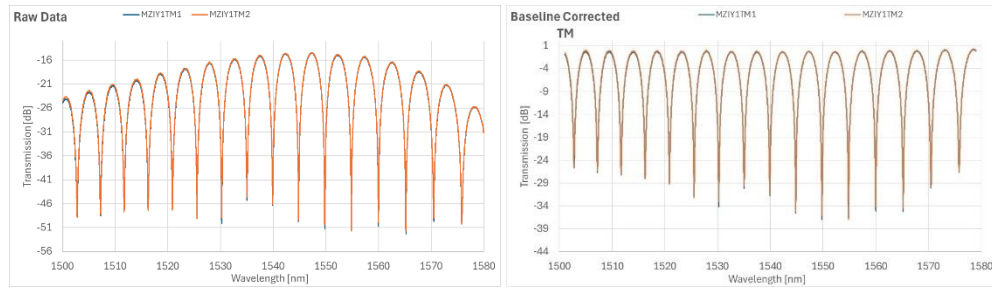


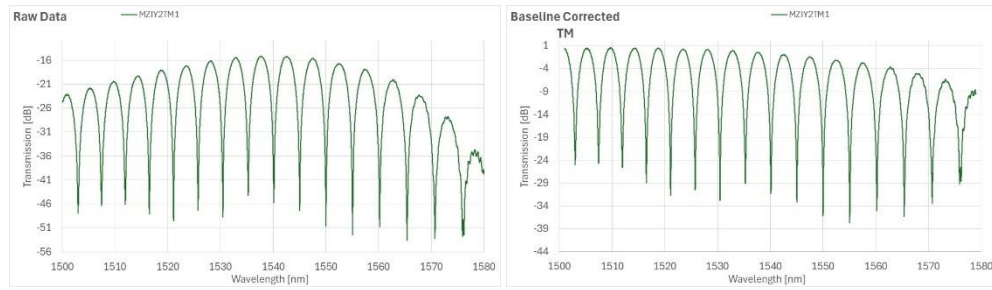
Fig. 31 GCbtoBTM loopback spectral measurements

5.2.2 MZIYTM

Device MZIY2TM could have been measured only on one direction to detector3. The measurement on the reverse direction from Laser to Dectector2 failed. I do not have yet an explanation.



(a) raw data (b) baseline corrected
Fig. 32 MZIY1TM spectral measurements (a) raw data, (b) baseline corrected



(a) raw data (b) baseline corrected
Fig. 33 MZIY2TM spectral measurements (a) raw data, (b) baseline corrected

6. Analysis

The main objective of the data analysis is to extract the waveguide parameters such as effective index and group index.

Two fitting methods have been proposed:

- Findpeaks:
 - Look for the minima in the spectra (log scale is easier)
 - Calculate the FSR vs λ for the ΔL of the interferometer and derive the group index n_g according to (12)
 - Find the effective index n_{eff} to match in the middle of the spectra one of the peak of the fitted curve to the measurement
- Autocorrelation:
 - From data autocorrelation, estimate the periodicity of the spectrum to calculate FSR vs λ
 - Derive n_g from (12) and determine the transfer function from the periodicity
 - Adjust n_{eff} to offset horizontally the fitted function to match measurement data. This done by cross correlating simulation and measurement.

I used the MatLab codes provided in the course, thank you. First, I wanted to compare both methods, but Findpeaks one was not successful on all my measurement data set.

An example of the Autocorrelation method is shown in Fig. 34.

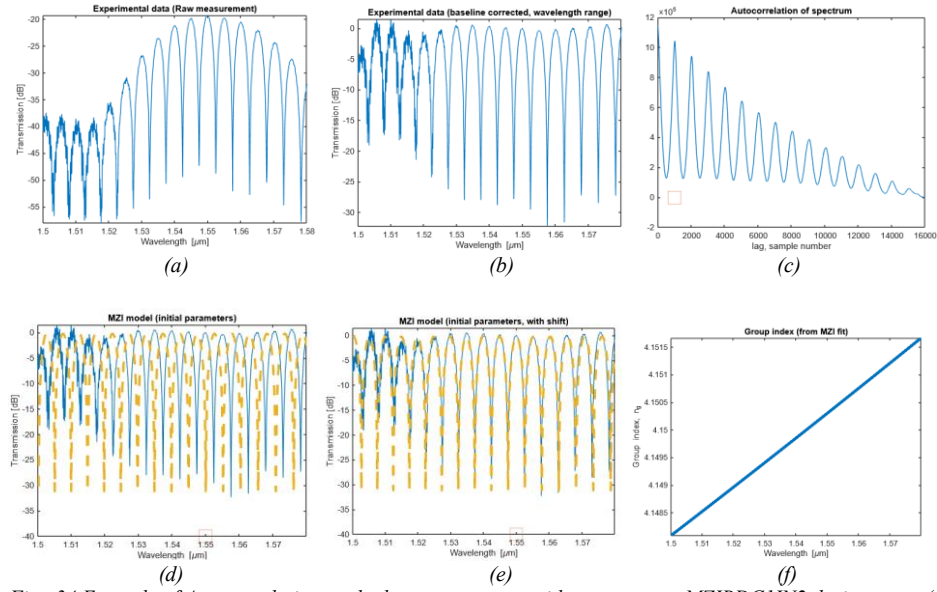


Fig. 34 Example of Autocorrelation method to extract waveguide parameters, MZIBDC1IN2 device, steps (a) to (f)

Table 8 summarises the analysis of FSRs and group indexes performed at 1550nm on the measurements data provided after the device fabrication. Results fully match with Monte-Carlo simulations. All MZIBDC exhibit a group index slightly lower than Corner Analysis limit leading to FSR slightly higher. It might be due to bad settings for the Corner Analysis or a wrong calculation from the measured data.

Table 8 Comparison of measured group indexes & FSR to Monte-Carlo simulation and Corner Analysis (at 1550nm)

λ_0 1550nm	Measurement data analysis Autocorrelation technic				Monte-Carlo (4 wafer, 15 locations)				Corner analysis			
	Detector #	neff	FSR [nm]	ng	ng min	ng max	FSR min	FSR max	ng min	ng max	FSR min	FSR max
MZIY1TE1	3	2,4053	5,02	4,189	3,947	4,457	4,72	5,33	4,175	4,255	4,94	5,04
MZIY1TE2	2	2,4053	5,02	4,188								
MZIY2TE1	3	2,4197	5,03	4,186								
MZIY2TE2	2	2,4197	5,03	4,184								
MZIBDC1IN2	3	2,4020	5,07	4,150	3,992	4,267	4,93	5,27				
MZIBDC1IN3	1	2,3952	5,07	4,151								
MZIBDC1IN3	2	2,4020	5,07	4,150								
MZIBDC2IN2	3	2,4043	5,07	4,150								
MZIBDC2IN3	1	2,3975	5,07	4,149								
MZIBDC2IN3	2	2,4043	5,07	4,150								
Michelson1In1	3	2,3977	5,05	4,166	3,659	5,380	3,91	5,75				
Michelson1In2	2	2,3978	5,05	4,166								
Michelson2In1	3	2,4121	5,04	4,175								
Michelson2In2	2	2,4121	5,04	4,174								
MZIY1TM1	3	2,3976	5,02	3,728	3,700	4,001	4,68	5,06	3,511	3,867	4,84	5,33
MZIY1TM2	2	2,3976	5,02	3,729								
MZIY2TM1	3	2,3981	5,02	3,730								

Let us estimate the FSR with another simpler method. Knowing the expected FSR, we can look for consecutive minimum and maximum directly on raw data without any smoothing. Then n_g is derived from (12). We could call this method as “Raw peaks”.

Table 9 shows that Michelson interferometers do not fit well with Corner analysis. But the difference between the two FSR calculation methods is weak as shown in Table 10. Therefore, one can expect that the issue comes from the Corner Analysis.

Table 9 Comparison of the measured group index from “Raw peaks” method to Monte-Carlo simulation and Corner Analysis

λ_0 1550nm	Measurement data analysis			Monte-Carlo				Corner analysis			
	Detector #	FSR [nm]	ng	(4 wafer, 15 locations)				ng min	ng max	FSR min	FSR max
MZIY1TE1	3	5,01	4,195	3,947	4,457	4,72	5,33	4,175	4,255	4,94	5,04
MZIY1TE2	2	5,02	4,195								
MZIY2TE1	3	5,04	4,174								
MZIY2TE2	2	5,04	4,177								
MZIBDC1IN2	3	5,04	4,172	3,992	4,267	4,93	5,27				
MZIBDC1IN3	1	5,07	4,151								
MZIBDC1IN3	2	5,03	4,184								
MZIBDC2IN2	3	5,01	4,203								
MZIBDC2IN3	1	5,04	4,173								
MZIBDC2IN3	2	5,09	4,136								
Michelson1In1	3	5,08	4,145	3,659	5,380	3,91	5,75				
Michelson1In2	2	5,08	4,141								
Michelson2In1	3	5,05	4,170								
Michelson2In2	2	5,06	4,158								
MZIY1TM1	3	5,01	3,736	3,700	4,001	4,68	5,06	3,511	3,867	4,84	5,33
MZIY1TM2	2	5,02	3,733								
MZIY2TM1	3	5,01	3,736								

Table 10 FSR and group index calculation method comparison

λ_0 1550nm	Detector #	Raw peaks method vs Autocorrelation	
		FSR [nm]	ng
MZIY1TE1	3	-0,008	0,007
MZIY1TE2	2	-0,008	0,006
MZIY2TE1	3	0,015	-0,012
MZIY2TE2	2	0,009	-0,007
MZIBDC1IN2	3	-0,027	0,022
MZIBDC1IN3	1	-0,001	0,000
MZIBDC1IN3	2	-0,041	0,034
MZIBDC2IN2	3	-0,064	0,053
MZIBDC2IN3	1	-0,030	0,024
MZIBDC2IN3	2	0,017	-0,014
Michelson1In1	3	0,025	-0,021
Michelson1In2	2	0,030	-0,025
Michelson2In1	3	0,006	-0,005
Michelson2In2	2	0,019	-0,016
MZIY1TM1	3	-0,011	0,008
MZIY1TM2	2	-0,007	0,005
MZIY2TM1	3	-0,008	0,006

A last analysis has been performed on the ER. MZI with Y splitters and Michelson structures seem to have similar ER behaviour. Fig. 35 seems to confirm that Interferometric structures made with Y-Branched have a higher extinction Ratio than with Broadband Directional

Couplers. At least, measurements were good enough to enable this ER analysis. A theoretical study would be of interest for me.

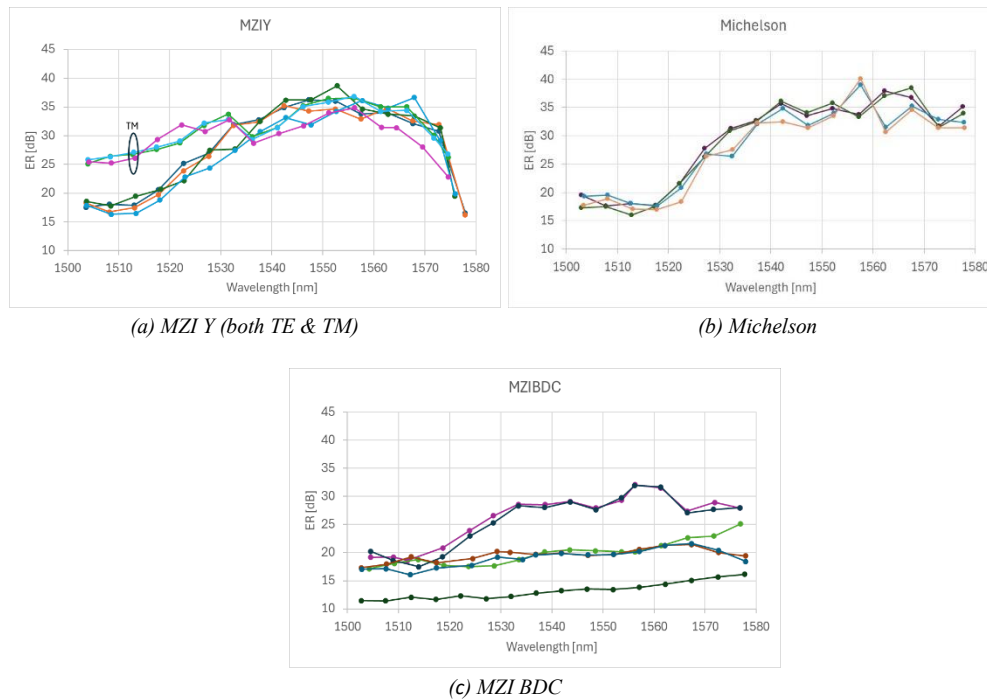


Fig. 35 Measured Extinction Ratio plotted by interferometer type, (a) MZI Y, (b) Michelson and (c) MZI BDC

7. Conclusion

This course allowed me to apprehend elementary processes to simulate, design, manufacture and characterise Photonic Integrated Circuits. Performance variabilities could come from design approximation, process variation, measurement accuracy and environmental conditions. Packaging might also impairs. The study on simple devices in this report allowed me to feel how much PIC design and manufacture is challenging. Nevertheless, it has already moved to mass production by some industrial companies.

Also, it came to evidence for me that Electron Beam Lithography is well adapted for niche applications where volume in production are as low as few hundred units per year. It is also a very fast and cheaper way to get some PIC prototypes.

8. Acknowledgment

I strongly acknowledge the edX UBCx Phot1x Silicon Photonics Design, Fabrication and Data Analysis course, which is supported by the Natural Sciences and Engineering Research Council of Canada (NSERC) Silicon Electronic-Photonic Integrated Circuits (SiEPIC) Program. The devices were fabricated by Richard Bojko at the University of Washington Washington Nanofabrication Facility, part of the National Science Foundation's National Nanotechnology Infrastructure Network (NNIN), and Cameron Horvath at Applied Nanotools, Inc. Enxiao Luan performed the measurements at The University of British

Columbia. We acknowledge Lumerical Solutions, Inc., Mathworks, Mentor Graphics, Python, and KLayout for the design software.

Finally, a special thanks to Lukas Chrostowski and Mateo Branion their online support and especially for the high quality of this course.

References

- [1] M. W. Geis, S. J. Spector, R. C. Williamson et al., "Submicrosecond Submilliwatt Silicon-on-Insulator Thermo-optic Switch", IEEE Photonics Technology Letters, vol. 16, no.11, November 2004
- [2] P. Sun, R.M. Reano, "Submilliwatt thermo-optic switches using free-standing silicon-on-insulator strip waveguides", Optics Express, Vol. 18 issue 8, pp. 8406-8411 (2010), <https://doi.org/10.1364/OE.18.008406>
- [3] X. Tu et al., "50Gb/s silicon optical modulator with travelling-wave electrodes", Optics Express, Vol. 21, No. 10, pp. 12776-127782 (2013), <https://doi.org/10.1364/OE.21.012776>
- [4] L. Yang, S. Wang, F. Kong et al., "Design of Traveling-Wave Electrode for Silicon Mach-Zehnder Electro-Optic Modulator", [2021 IEEE 4th International Conference on Electronic Information and Communication Technology \(ICEICT\)](#)
- [5] X. Fu, H. Jia, S. Shao et al., Silicon Photonic Wavelength (De-)Multiplexer for Low-loss Flat-passband DWDM Applications", [2018 Asia Communications and Photonics Conference \(ACP\)](#)
- [6] S-H Jeong, "Broadband 1×8 channel silicon-nanowire-waveguide WDM filter based on point-symmetric Mach-Zehnder interferometric optical couplers in the O-band spectral regime", Vol. 2, Issue 12, pp. 3564-3575 (2019), <https://doi.org/10.1364/OSAC.2.003564>
- [7] L. Chrostowski, M. Hochberg, "Silicon Photonics Design: From Devices to Systems", Cambridge University Press, 2015
- [8] Z. Lu, U. Yun, Y. Wang et al., "Broadband silicon photonic directional coupler using asymmetric-waveguide based phase control", Optics Express, Vol. 23, No. 3, pp. 3795-3808 (2015), <https://doi.org/10.1364/OE.23.003795>
- [9] L. B. Soldano, E. Pennings, "Optical Multimode-Interference Devices Based on Self-Imaging: Principles & Applications", Journal of Lightwave Technology, Vol. 13, No. 4, Invited Paper, April 1995
- [10] R. Song, J. Sun, J. Wang et al., "High-speed compact folded Michelson interferometer modulator", Optics Express, Vol. 30, Issue 13, pp. 23704-23715 (2022), <https://doi.org/10.1364/OE.460579>
- [11] D. Patel, V. Veerasubramanin, S. Gosh et al., "High-speed compact silicon photonic Michelson interferometric modulator", Optics Express, Vol. 22, Issue 22, pp.26788-26802 (2014), <https://doi.org/10.1364/OE.22.026788>
- [12] Ansys Lumerical MODE software, <https://www.ansys.com/products/optics/mode>
- [13] Ansys Lumerical INTERCONNECT software, <https://www.ansys.com/products/optics/interconnect>
- [14] KLayout software, <https://www.klayout.de/intro.html>
- [15] Integrated Photonics Foundry, Applied Nanotools, <https://www.appliednt.com>